ADVANCED FUNCTIONAL MATERIALS

# Supporting Information

for *Adv. Funct. Mater.,* DOI: 10.1002/adfm.201806772

## Discrete-Continuum Duality of Architected Materials: Failure, Flaws, and Fracture

*Arturo J. Mateos, Wei Huang, Yong-Wei Zhang,* and Julia R. Greer**

# Supporting Information

## Discrete-continuum duality of architected materials: failure, flaws, and fracture

**Arturo J. Mateos**[a], **Wei Huang**[b], **Yong-Wei Zhang**[c], **and Julia R. Greer**[a]

[a]Division of Engineering and Applied Science, California Institute of Technology, Pasadena, CA 91125; [b]School of Aeronautics, Northwestern Polytechnical University, Xi'an, China, 710072; [c]Institute of High Performance Computing, A*STAR, Singapore, 138632

### 1. Fabrication

A multi step fabrication process is employed to fabricate nanomechanical tensile specimens; as illustrated in Fig. S1. Fabrication of all samples starts with the writing of a polymer sample made out of photoresist (IP-Dip) using two-photon lithography (TPL) direct laser writing (DLW) in a Photonic Professional lithographic system (Nanoscribe GmbH). Samples are written using laser powers in a range from 15-20 $mW$ and a writing speed of 20000-50000 $\mu m/s$. The laser power is used to control the effective diameter of the tubes, and the speed varies slightly during the writing process to control the quality of the supporting structures.

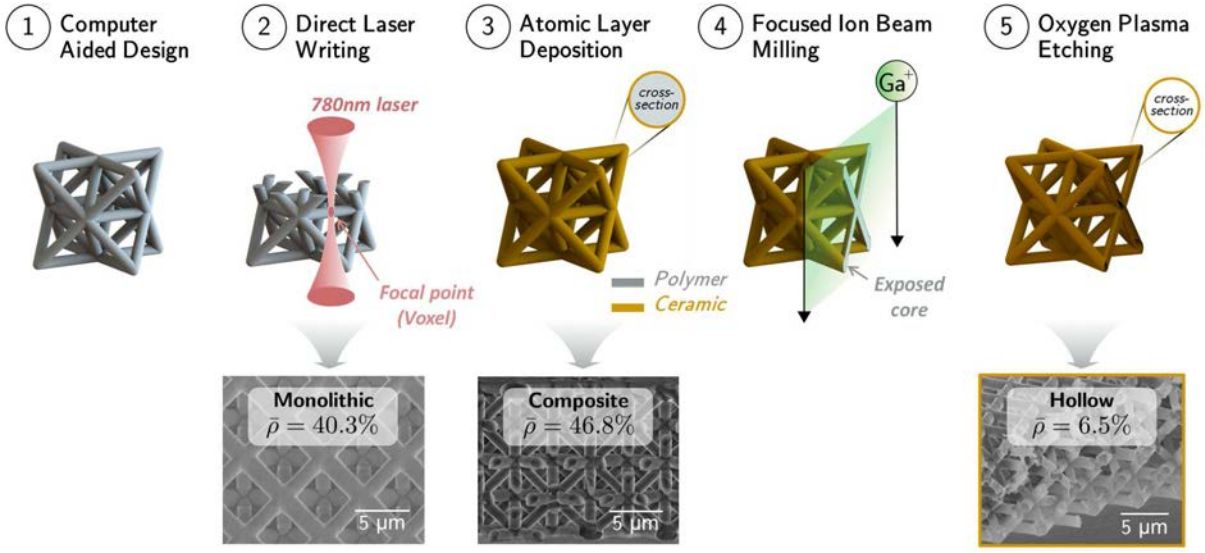


**Fig. S1.** Complete step-by-step fabrication process employed to create hollow tube tensile specimens.

The resulting polymeric sample is then critically-point dried with a Autosamdri 931 (Tousimis) and conformally coated with 50$nm$ of aluminum oxide (alumina) using atomic layer deposition (ALD). Deposition is done at 150°$C$ in a Cambridge Nanotech S200 ALD system using the following steps: H2O is pulsed for 15ms, the system is purged for 20s, trimethyl aluminum (TMA) is pulsed for 15ms, the system is purged for 20s, and the process is repeated. The carrier gas is nitrogen, which is used at a flow rate of 20$sccm$. The process was repeated for 500 cycles to obtain the desired thickness coating. The thickness of the coatings was verified using spectroscopic ellipsometry with an alpha-SE Ellipsometer (J.A. Wollam Co., Inc.).

After deposition, a focused ion beam (FIB) (Versa 3D DualBeam, FEI) is used to mill away auxiliary beams of the sample to expose the polymer to air, as shown in Fig. S2. Once the polymer is exposed, samples are placed into a SP100 oxygen plasma system (Anatech Ltd.) for 50-80 hours at a pressure of 100$mTorr$ and at 100$W$ of power in order to remove the polymer from the gauge section. It is possible to

determine whether the polymer has been fully etched away by looking for any contrast change in the beams using a scanning electron microscope, as shown in Fig. S3. For tensile specimens, it is crucial to regularly measure the etching profile to prevent structural damage of the supporting structures.

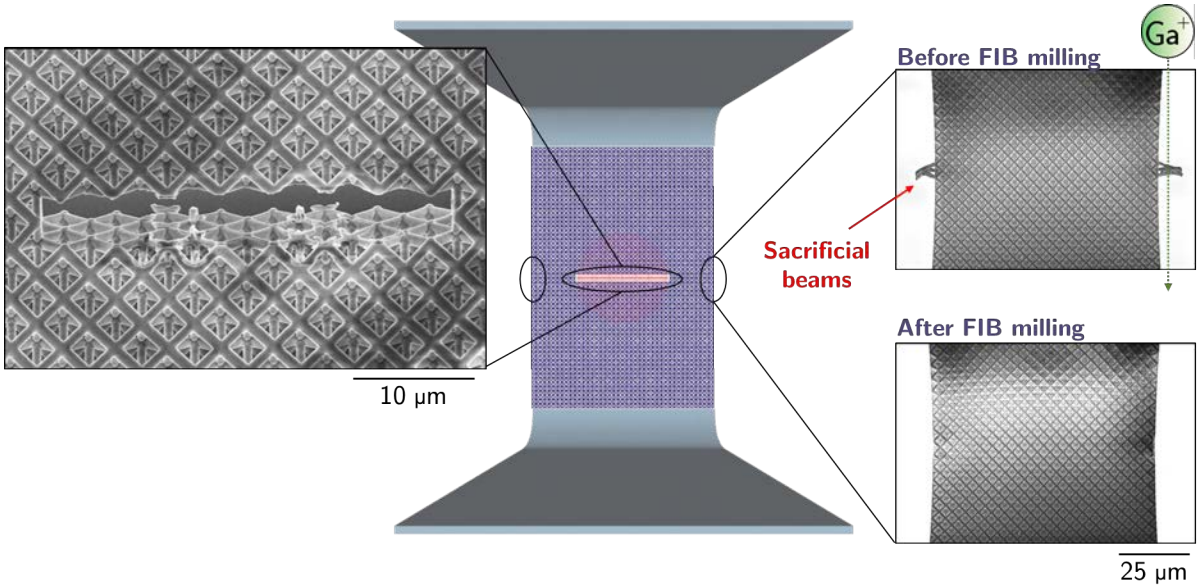


**Fig. S2.** Focused Ion Beam (FIB) milling is employed to expose the polymeric core by removing sacrificial beams.

**Etching profile.** To expose the polymer core and etch it away, auxiliary struts were milled by focused-ion beam (FIB) milling to provide an opening for oxygen plasma to ash the polymer using a SP100 oxygen plasma system (Anatech Ltd.) (Figs. S2-S3). The addition of auxiliary struts enables the exposure of the internal polymer with minimal ion bombardment to sacrificial material and no damage in critical regions of the sample, such as the vicinity of the notch root. Excessive ion bombardment could induce material and geometric defects, such as changes in the material composition and introduce external flaws in the form of missing struts or nodes. The final sample consists of a ceramic hollow-tube gauge section supported by polymer-alumina composite structures.

**Sample Survival Rate.** There are several critical steps in the fabrication process that reduced the sample survival rate. More than 1000 samples were successfully written on silicon substrates but $\sim 114$ samples were used during the analysis of this work. Most samples were successfully developed, critically point dried, and coated with ALD alumina. Sacrificial beams and a pre-defined notch allowed for a high survival rate after focused ion beam milling; which enabled identical samples regardless of the presence of a notch or notch orientation. The survival rate after the etching process was low ($\sim 10\%$) making this the critical step in the fabrication process. The low survival rate is mostly due to the high probability of finding an unwanted defect in the alumina thin film which lets $O_2$ plasma etch the substrate at undesirable locations. For example, if a defect (in the form of a crack or void) is located at the interface between the bottom support and the substrate, then etching will simultaneously start at the gauge section and at the bottom support. Since the etching rate is higher for the support compared to the tortuous paths of the gauge section, then the support will be completely hollowed out before the gauge section is ready for the tension experiment. A

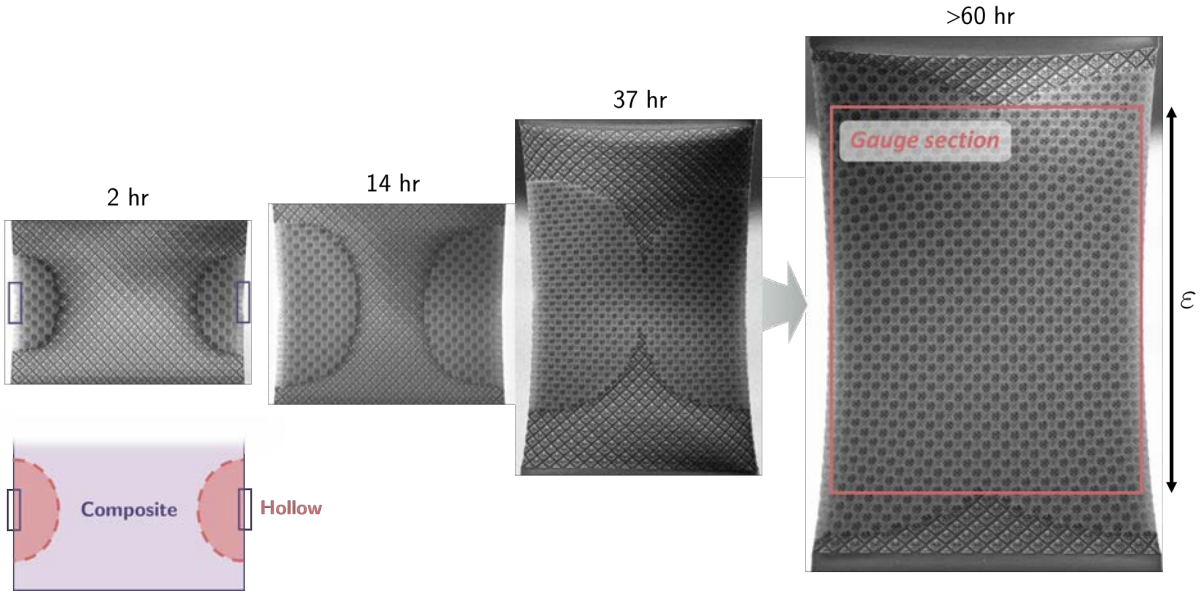


**Fig. S3.** Etching profile. Sacrificial beams are removed from both sides of the gauge section to expose the polymer core to oxygen plasma. The duration of the etching process depends on the number of openings and the distance between the openings and the wavefront of polymer. Afterwards, the gauge section consists of hollow alumina tubes.

visual inspection of the supports with a microscope does not necessarily allow the determination of failed samples, which leads to evaluating the integrity of the samples during the testing phase. The minimum hours required to fabricate an tension specimen with an architected gauge section is $> 84.5\ hr/sample$, as listed in Table S1.

**Table S1. Duration of each step during the fabrication process and testing phase.**

| # | Process | Duration | Approx. survival rate |
|---|---|---|---|
| 1 | Substrate preparation | 1 $hr/sample$ | 99% |
| 2 | Two-photon lithography | 4 $hr/sample$ | 90% |
| 3 | Resin development | 0.5 $hr/sample$ | 90% |
| 4 | Critical point drying | 1 $hr/sample$ | 90% |
| 5 | Thin film deposition | 6 $hr/sample$ | 90% |
| 6 | Focused ion beam milling | 1 $hr/sample$ | 90% |
| 7 | $O_2$ plasma etching | $>$ 70 $hr/sample$ | 10% |
| 8 | Tension experiment | 1 $hr/sample$ | 80% |
| | TOTAL | $>$ 84.5 $hr/sample$ | 10% |

## 2. Center-notched tension design for architected materials

Adequate consideration of sample design must be taken into account for a proper tensile test, at any length scale. The sample design must prevent induced stress concentrations and premature failure initiation sites, introduced by the required supporting structures bracing the gauge section. The nanolattices in this work were designed to emulate conventional conditions for fracture experiments in monolithic materials, where samples take a dog-bone shape with a central gauge section of uniform width. The gauge section is braced by a bottom support attached to the substrate and a top support that engages with a custom-made tension grip in an in-situ nanomechanical instrument (InSEM, Nanomechanics Inc.). The supports were designed to minimize the stress concentrations and premature failure initiation at their interfaces with the gauge section. The gauge section contains 918 octet unit cells (27 (height, H) x 17 (width, W) x 2 (thickness, B)). The as-fabricated dimensions consist of an average unit cell length of $4.72 \pm 0.03 \mu m$, an average outer tube radius of $491nm \pm 62nm$ with eccentricity of 1.1, and alumina tube wall thicknesses of $50nm$.

The gauge section geometry was generated using MATLAB scripts and the supporting structures were designed using a CAD model generated with Solidworks (Dassault Systèmes). These CAD models were also used to determine the relative density of the samples. The notch geometry was designed to resemble naturally occurring cracks in lattices. For materials with lattice architectures, notches come in the form of a combination of structural imperfections; such as unconnected or broken struts and missing nodes. We fabricated some of the samples to contain a pre-defined through-thickness notch, which was composed of a collection of omitted tubes with relative notch lengths of $2a/W = 0.45$ and notch orientations varying from 0 to 90 degrees with respect to the direction of loading. Notch orientations are related to the in-plane cubic symmetry of the octet ranging from 0 to 90 degrees; that is, $\beta = \arctan(i) \cdot \left(\frac{180}{\pi}\right)$ where $i = [0, 0.5, 1, 2, 8, \infty]$. The addition of the notch to the pre-defined gauge section designs provides consistent means of fabricating nearly identical samples. The designs were used as input to the lithographic instrument. A visual representation of the notch generating scripts is provided with *Video S3*.

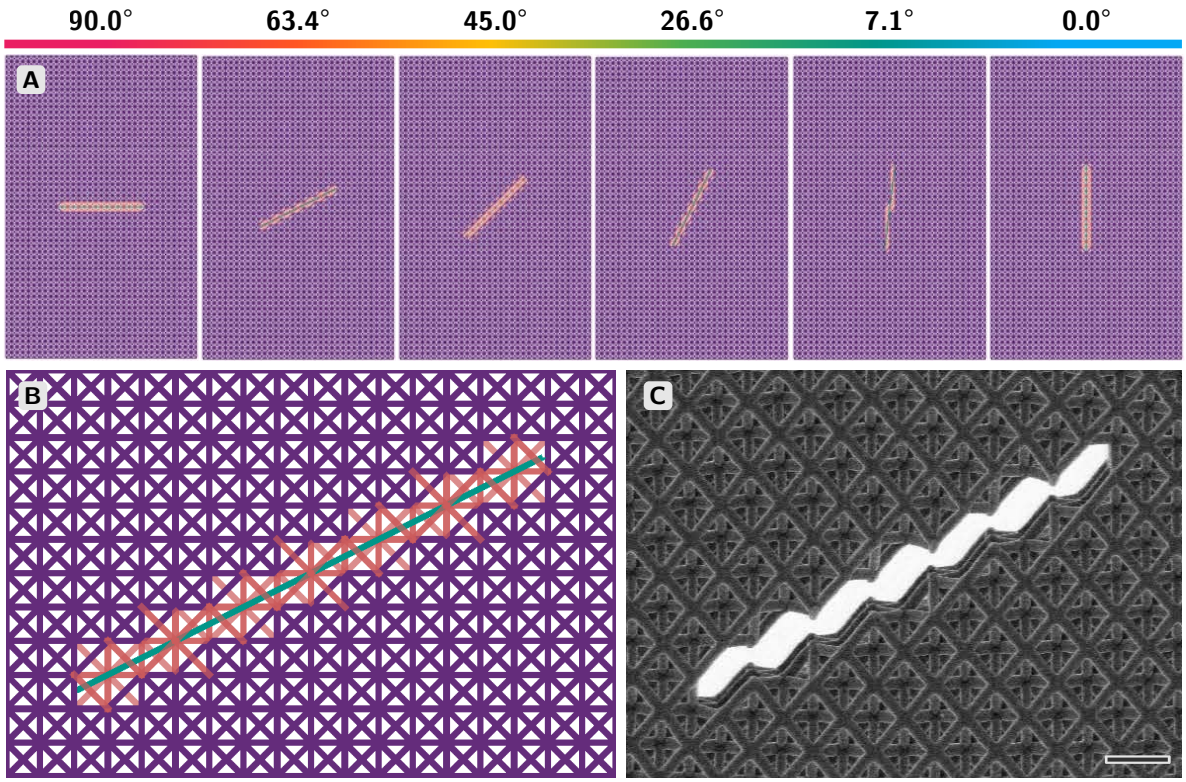


**Fig. S4.** Center-notch geometry generated by MATLAB scripts. (A) Architected gauge sections of notched samples contain a pre-defined through-thickness notch composed of a collection of omitted tubes and nodes with relative notch lengths of $2a/W = 0.45$ and notch orientations varying from 0 to 90 degrees with respect to the direction of loading. (B-C) Close-up MATLAB image of notch oriented at 63.4 degrees and corresponding SEM image of final sample.

## 3. Nanomechanical experimental setup

Uniaxial tension experiments were conducted in an in-situ nanomechanical instrument (InSEM, Nanomechanics Inc.) to observe global and local failure behavior. Samples were subjected to an applied tensile load at a quasi-static strain rate of $10^{-3}s^{-1}$ by engaging with a custom-made tension grip. The tension grip was machined on the head of a $0.8mm$ stainless steel screw by electrical discharge machining, see Fig. S5. *Video S1* and *Video S2* show the in-situ mechanical data and its corresponding real-time video of the deformation of an unnotched and notched specimen.

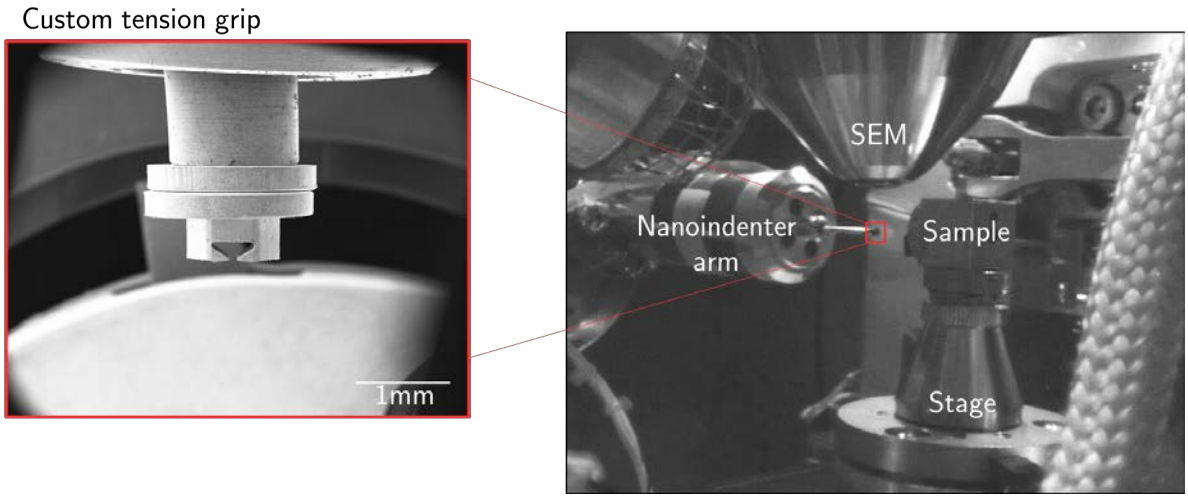


**Fig. S5.** Custom tension grip used to test nano-architected tensile samples.

## 4. Data Analysis Methods

To correctly measure the uniaxial tensile properties of a material, special techniques must be adopted in order to avoid damaging samples and compromising the area of interest. However, the additional material that must be used to grip, support, or adhere the sample, will lie in the loading path and influence the recorded strain measurements. The contributions from these sources must be accounted for to accurately report the strains of the area of interest. The extension from outside the gauge section must be determined and subtracted from the total measured extension. The total measurement of the stiffness for the nanomechanical experiments can be viewed as the effective stiffness of springs in series, as illustrated in Fig. S6A and quantified as

$$\frac{1}{K_{eff}} = \frac{1}{K} + \frac{1}{K_s} \quad [1]$$

where $K_{eff}$ is the effective stiffness recorded by the nanomechanical instrument, $K$ is the stiffness of the gauge section, and $K_s$ is the stiffness outside of the gauge section, as shown in Fig. S6B. Since compliance is the inverse of stiffness, Eq. 1 can be written as

$$C_{eff} = C + C_s \quad [2]$$

Additional experiments on samples without the gauge section were performed to determine $C_s$. Samples were fabricated without the hollow gauge section, as shown in Fig. S6C. Two layers of alumina-polymer core-shell composite octet unit cells make up the central section of these samples to resemble the few composite unit cells in samples with complete hollow gauge sections. The average compliance of multiple samples was determined and subtracted from the displacement and subsequent strain calculations for each unnotched and notched sample. The corrected displacements were then normalized by the gauge section length to determine engineering strains. The corresponding loads for all samples were converted to stresses, defined as $\sigma = P/A$; $P$ is the measured load and $A$ is the total cross-sectional area perpendicular to the load.

Displacements and strains of the gauge section could also be calculated using the observed length change with the real-time deformation video recorded by the scanning electron microscope. However, since the window frame of the video must account for the entire gauge section ($\sim 120\mu m$ in length) and total strain

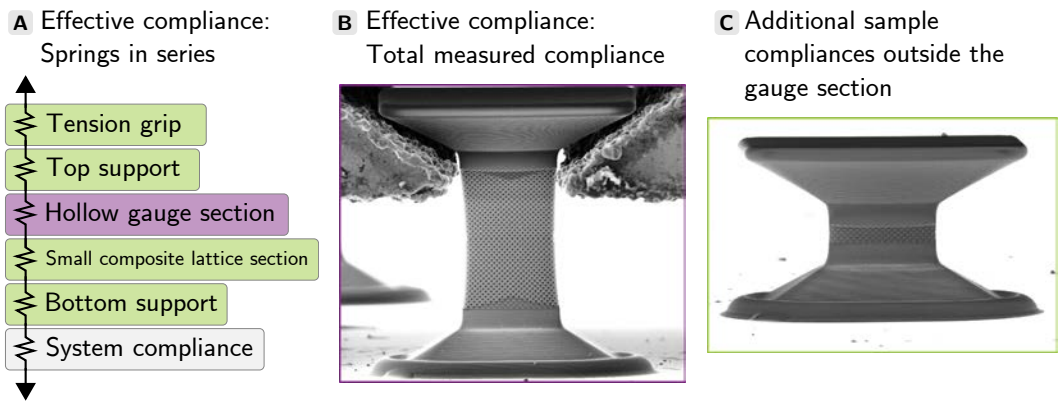


**Fig. S6.** Displacement and strain for the hollow gauge section only can be obtained by subtracting the contribution of the additional compliance from the effective compliance recorded by the nanomechanical instrument.

at failure of $0.01 - 0.03$ ($\sim 1 - 3\mu m$), the maximum length change is confined to less than 5 pixels. This low amplitude of displacements and the characteristic grainy appearance of micrographs (as a result of random fluctuations of electrons in the electron beam) render the video-assisted technique unsuitable for accurate strain measurements. Fig. S7 illustrate a comparison between the compliance-corrected data and the video-corrected data. Displacements corrected with the real-time video resulted in stiffer samples by more than a factor of 2 compared the compliance-corrected data, which yielded stiffnesses close to the values reported for similar hollow-tube octet nanolattices tested in compression (6). The compliance method was employed to accurately measure the displacements and strains of the gauge section, and to systematically account for the additional compliance by the sample geometry and nanomechanical system.

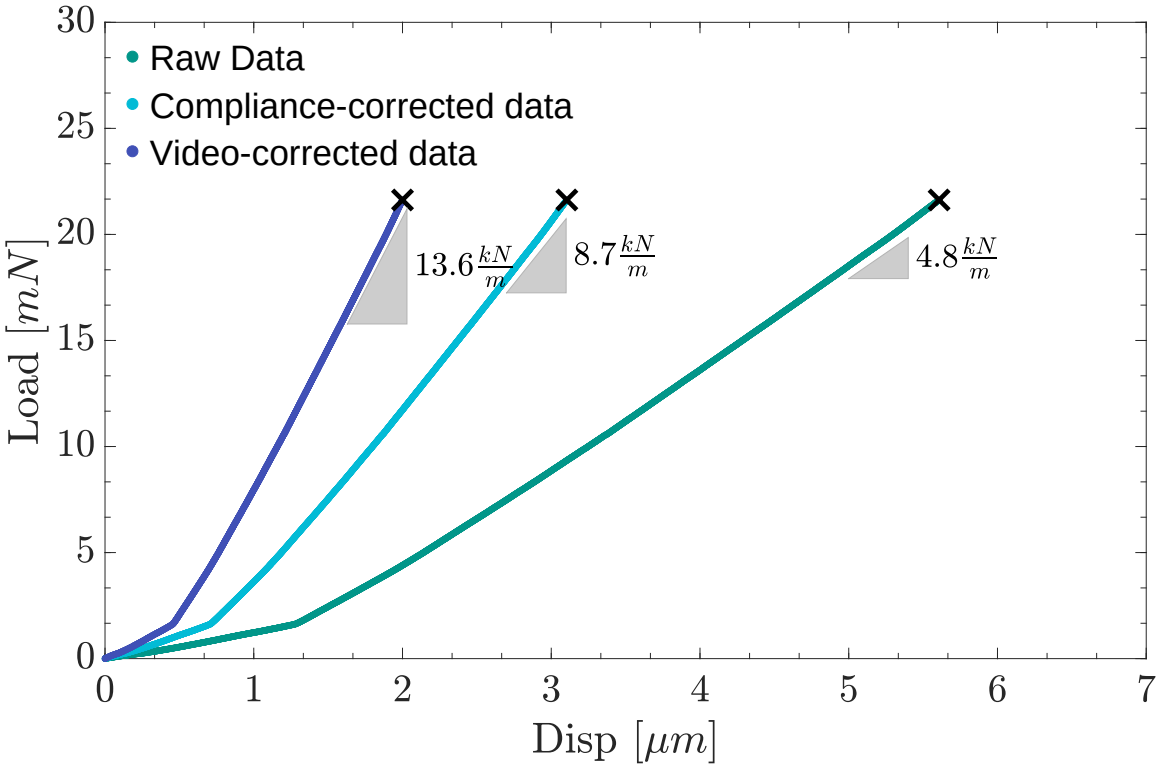


**Fig. S7.** Comparison between raw data, compliance-corrected data, and video-assisted corrected data.

## 5. Stiffness analysis

The stiffness of a linear-elastic solid plate under the same geometric constraints as the samples in this study can be predicted as a function of notch orientation. Assuming linear elasticity, the compliance of a cracked plate under tension is related to the strain energy release rate $G$ by

$$G = \frac{P^2}{2B}\frac{\partial C}{\partial a} \quad [3]$$

where $P$ is the applied tensile load, $B$ is the width of the sample, $C$ is compliance, and $a$ is half the crack length. Under plane stress, the strain energy release rate is proportional to the square of the in-plane stress intensity factors $K_I$ and $K_{II}$ as the crack orientation varies,

$$G = \frac{K_I^2 + K_{II}^2}{E} \quad [4]$$

Using Eq. 9a and Eq. 9b as the definition of $K_I$ and $K_{II}$, Eq. 3 can be solved for the compliance of a linear-elastic cracked solid as a function of material properties and sample dimensions, which is found to be

$$C = \frac{H}{EBW}\left[1 + 2\pi\frac{W}{H}\left(\frac{a}{W}\right)^2 \cos^2\beta\right] \quad [5]$$

This calculation is compared to the experimental stiffness data in this study, shown in Fig. S8. The average material properties and global dimensions used for this calculation is listed in Table S2.

**Table S2. Effective material properties and geometric constants used for computing the stiffness of an equivalent linear elastic plate as a function of notch orientation**

| Parameter | Value |
|---|---|
| Unit cell length, L | 5 $\mu m$ |
| Gauge section depth, B | (2 x L) $\mu m$ |
| Gauge section width, W | (17 x L) $\mu m$ |
| Gauge section height, H | (27 x L) $\mu m$ |
| Crack length, a | 19.45 $\mu m$ |
| Young's Modulus, E | 1.30 $GPa$ |

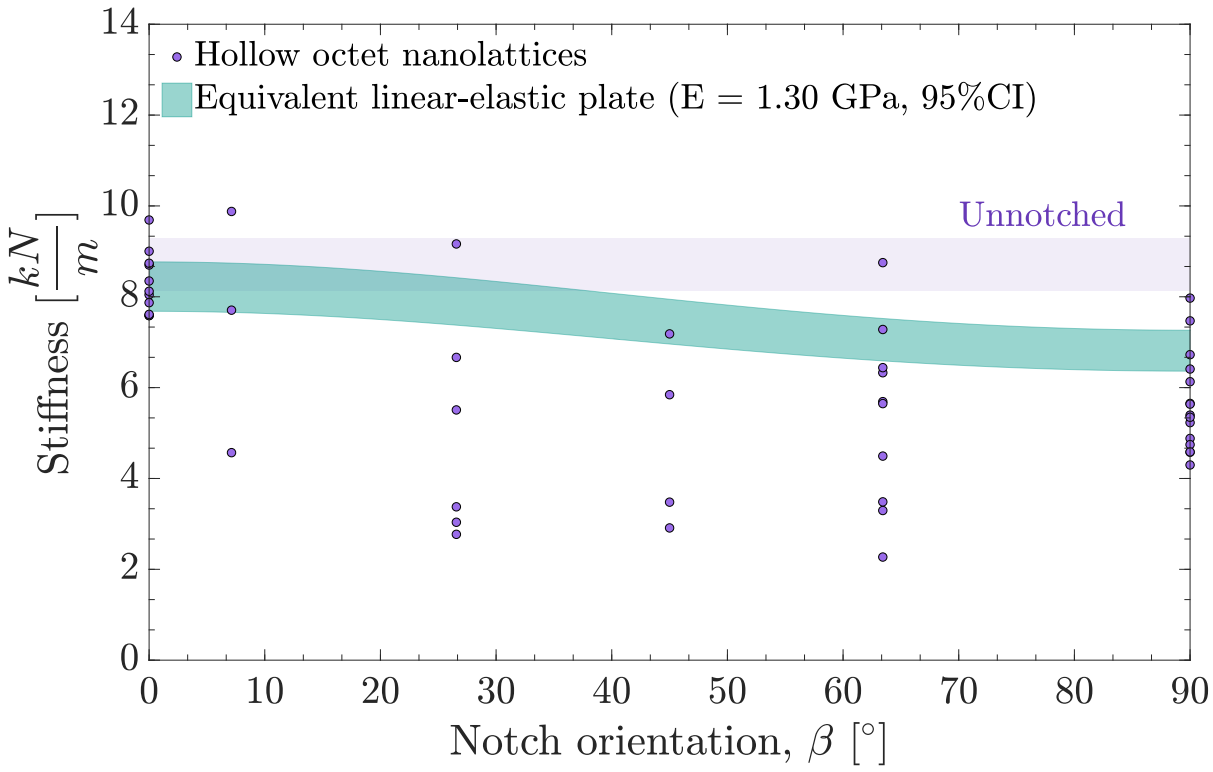


**Fig. S8.** Stiffness for hollow octet nanolattices tested in this study and that of an equivalent linear-elastic solid as a function of notch orientation. The stiffness for the unnotched samples are also plotted as a band corresponding to a $95\%$ confidence interval centered at the mean stiffness for all unnotched samples.

Using this approach, it appears that the specimens with the highest failure strength follow the expected trend in stiffness of the equivalent continuum plate as a function of notch orientation. The failure strength of samples exhibiting low stiffness is misleading as minor misalignment of the experimental setup can induce non-uniform deformation and inhomogeneous loading. Common to tensile experiments of brittle materials, the sources and magnitude of scatter in strains among geometrically indistinguishable specimens are attributed to experimental misalignment that contribute to an initial low stiffness region and premature failure.

## 6. Cyclic tensile loading

The stress-strain data for all unnotched center-notched tensile specimens is shown in Fig. S9. For clarity, only one representative curve is colored and all others are grayed out. The data reveals that after the initial self-alignment into the tensile grips (shown by the non-linear behavior within 1% strain of incipient loading), all specimens displayed linear elastic loading up to failure regardless of the presence of a notch (Video S1). The point of tensile failure strength is defined as the maximum tensile stress prior to failure and is denoted by 'x' in Fig. S9. The distribution of local nodal strengths leads to scatter in the observed tensile failure strengths. We calculated the elastic modulus from a linear fit of the stress-strain data after 50% of the maximum strain for all samples. We used bootstrap statistical analysis to calculate the mean and standard error of the elastic modulus for each notch orientation, which is shown by the dashed line to the right of the data. We found the elastic modulus of unnotched specimens to be $1.30 \pm 0.04 GPa$ in agreement with experimental studies of similar nanolattices under compression (6).

The elastic behavior of these nanolattices was reaffirmed by performing cyclic tensile experiments. Cyclic experiments consisted of 10 loading segments to $\sim 0.90\%$ of the average load at failure for all unnotched samples, followed by an unloading segment past the original position of the tension grip (Fig. S9). The load-displacement data shows stable hysteretic cycling behavior for all cycles. After each consecutive cycle, the sample recovered to the original height on unloading with minimal degradation; all subsequent cycles showed nearly complete recovery to this initial deformed position. The nanomechanical instrument could be the main reason for the hysteresis due to the displacement spring in the transducer, which has a notable effect over high loads and low displacement ranges. The hysteresis in each cycle may also be attributed to friction between the tension grip and the tensile sample, but its contribution is most likely minimal.

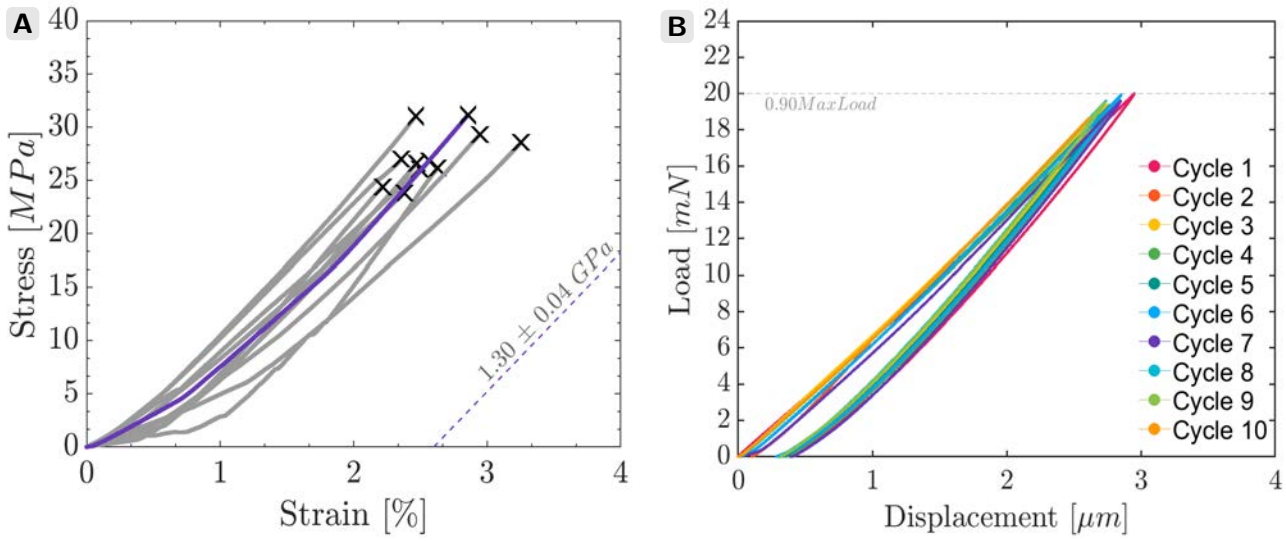


**Fig. S9.** Stress-strain response of unnotched samples. (A) The elastic modulus is averaged over all samples is also plotted and shown as a dashed line. For visual simplicity, one representative curve has been colored purple and all others keep in grey. (B) Cyclic loading of an unnotched sample. Minimal degradation of elastic properties is seen after 10 loading-unloading cycles.

## 7. Linear Elastic Fracture Mechanics (LEFM) Failure Criteria

**Maximum Circumferential Stress Criterion.** Classical fracture mechanics concepts have been used to predict the onset of failure and crack deflection of brittle materials (1–3). For a homogeneous, isotropic and linear-elastic brittle material, the in-plane stresses around the tip of a crack can be described in terms of the stress intensity factors ($K_I$ and $K_{II}$). The local stresses can be written in polar coordinates as,

$$\sigma_{rr} = \frac{1}{\sqrt{2\pi r}} \cos\frac{\theta}{2}\left[K_I\left(1+\sin^2\frac{\theta}{2}\right) + K_{II}\left(\frac{3}{2}\sin\theta - 2\tan\frac{\theta}{2}\right)\right] + T\cos^2\theta + O(r^{1/2}) \quad [6]$$

$$\sigma_{\theta\theta} = \frac{1}{\sqrt{2\pi r}} \cos\frac{\theta}{2}\left[K_I\cos^2\frac{\theta}{2} - \frac{3}{2}K_{II}\sin\theta\right] + T\sin^2\theta + O(r^{1/2}) \quad [7]$$

$$\tau_{r\theta} = \frac{1}{2\sqrt{2\pi r}} \cos\frac{\theta}{2}\left[K_I\sin\theta + K_{II}(3\cos\theta - 1)\right] - T\cos\theta\sin\theta + O(r^{1/2}) \quad [8]$$

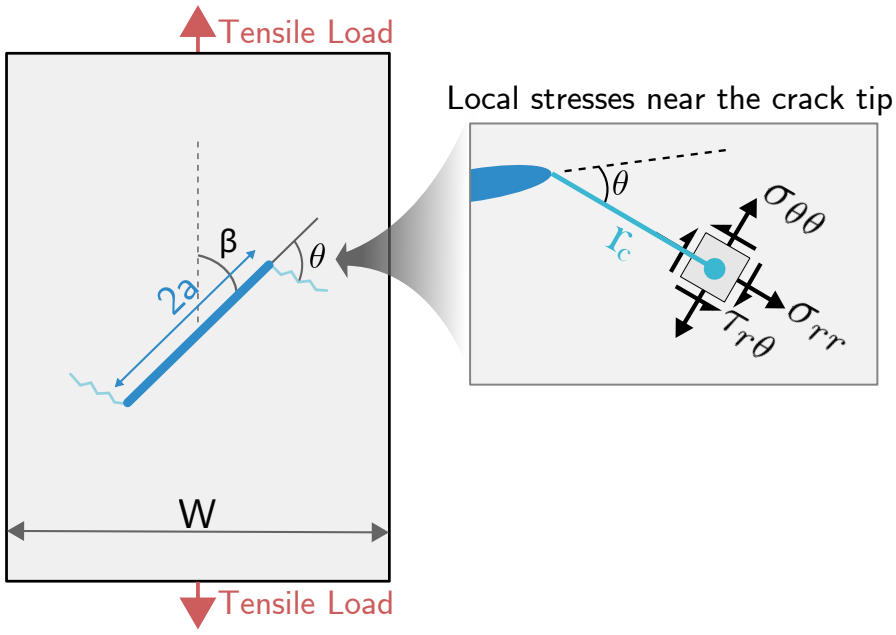


**Fig. S10.** Center-notched tension specimen geometry.

For a plate with a central crack of length $2a$ inclined at an angle $\beta$ with respect to the direction of loading and subjected to a uniaxial far-field tensile stress $\sigma$ (Fig. S10), the stress intensity factors are,

$$K_I = \sigma\sqrt{\pi a}\sin^2\beta \quad [9a]$$

$$K_{II} = \sigma\sqrt{\pi a}\cos\beta\sin\beta \quad [9b]$$

$$T = \sigma\sqrt{\pi a}\cos 2\beta \quad [9c]$$

$$K_{eff} = \sqrt{K_I^2 + K_{II}^2} \quad [9d]$$

According to Erdogan and Sih (4, 5), brittle fracture can be described by the criterion of maximum circumferential (or tangential) stress, which is based on two assumptions:

1. The crack propagates in radial direction $\theta_0$ perpendicular to the maximum circumferential stress $\sigma_\theta|_{max}$ (directional condition).
2. Crack propagation initiates when the near field stress $\sigma_\theta(\theta_0)$ at a distance $r_c$ in front of the crack tip reaches the same critical value as in pure mode I (failure condition).

Hence, the following failure and directional conditions define the onset of fracture,

$$\left.\frac{\partial \sigma_{\theta\theta}}{\partial \theta}\right|_{\theta_0} = 0 \quad [10]$$

$$\sigma_{\theta\theta}(\theta_0) = \frac{K_{Ic}}{\sqrt{2\pi r_c}} \quad [11]$$

Using Eq. 7 and Eq. 10, we obtain $\theta_0$ (at a distance $r_c$ from the crack tip),

$$\left.\frac{\partial \sigma_{\theta\theta}}{\partial \theta}\right|_{\theta_0} = \left[K_I \sin\theta_0 + K_{II}\left(3\cos\theta - 1\right)\right] - \frac{16}{3} T\sqrt{2\pi r_c}\sin\frac{\theta_0}{2}\cos\theta_0 = 0 \quad [12]$$

Once, the direction of fracture initiation has been found from Eq. 12, we can use Eq. 7 and Eq. 12 to determine the critical stress conditions at failure,

$$(\sigma_{\theta\theta})_c = \frac{1}{\sqrt{2\pi r}}\cos\frac{\theta_0}{2}\left[K_I\cos^2\frac{\theta_0}{2} - \frac{3}{2}K_{II}\sin\theta_0\right] + T\sin^2\theta_0 + O(r^{1/2}) \quad [13]$$

where $(\sigma_{\theta\theta})_c$ is the critical circumferential stress at a critical distance $r_c$. For pure mode I fracture when $K_{II}$, $T$, and $\theta_0$ are equal to zero, Eq. 13 reduces to

$$\sqrt{2\pi r_c}(\sigma_{\theta\theta})_c = K_{Ic} \quad [14]$$

where $K_{Ic}$ is the fracture toughness of the material. Therefore, the onset of fracture can be defined as

$$K_{Ic} - T\sqrt{2\pi r_c}\sin^2\theta_0 = \cos\frac{\theta_0}{2}\left[K_I\cos^2\frac{\theta_0}{2} - \frac{3}{2}K_{II}\sin\theta_0\right] \quad [15]$$

Thus, Eq. 10 and Eq. 15 define the onset of failure under mixed mode fracture (given a critical radius $r_c$, notch length $a$, and notch orientation $\beta$). The geometry of finite specimens has an effect on the crack tip stress fields, and so expressions for stress intensity factors must be modified by the addition of a correction factor to enable their use in practical applications (2). Hence,

$$K_c = Y\sigma_c\sqrt{\pi a} \quad [16]$$

In the case of center-notched tension specimens (2),

$$Y = \sqrt{\sec\frac{a}{W}} \quad [17]$$

**Direction of Fracture Initiation.** To solve for the initial deflection angle that dictates crack propagation trajectory, Eq. 12 is written as,

$$\begin{aligned}\left[K_I\sin\theta_0 + K_{II}\left(3\cos\theta - 1\right)\right] - \frac{16}{3}T\sqrt{2\pi r_c}\sin\frac{\theta_0}{2}\cos\theta_0 &= 0\\ \frac{K_I}{K_{eff}} + \frac{3\cos\theta - 1}{\sin\theta}\frac{K_{II}}{K_{eff}} - \frac{\frac{16}{3}T\sqrt{2\pi r_c}}{K_{eff}}\frac{\cos\theta_0\sin\frac{\theta_0}{2}}{\sin\theta_0} &= 0\\ \frac{K_I}{K_{eff}} + a\frac{K_{II}}{K_{eff}} &= b\end{aligned} \quad [18]$$

where,

$$a = \frac{3\cos\theta - 1}{\sin\theta} \tag{19a}$$

$$b = \frac{16}{3}\frac{T\sqrt{2\pi r_c}}{K_{eff}}\frac{\cos\theta_0 \sin\frac{\theta_0}{2}}{\sin\theta_0} = \frac{8}{3}B\alpha\frac{\cos\theta_0}{\cos\frac{\theta_0}{2}} \tag{19b}$$

and $B = \frac{T\sqrt{\pi a}}{K_{eff}}$ and $\alpha = \sqrt{\frac{2r_r}{a}}$. Now, by letting $z = \frac{K_{II}}{K_I}$, we can rewrite Eq. 18 to solve for $\theta_0$,

$$\frac{K_I}{\sqrt{K_I^2 + K_{II}^2}} + a\frac{K_{II}}{\sqrt{K_I^2 + K_{II}^2}} = b \tag{20}$$

$$\frac{1}{K_I\sqrt{K_I^2 + K_{II}^2}} + a\frac{1}{K_{II}\sqrt{K_I^2 + K_{II}^2}} = b \tag{21}$$

$$\frac{1}{\sqrt{1+z^2}} + a\frac{1}{\sqrt{\frac{1+z^2}{z^2}}} = b \tag{22}$$

Rearranging Eq. 22,

$$(a^2 + b^2)z^2 + 2az + (1 - b^2) = 0 \tag{23}$$

Solving Eq. 23 for $z$,

$$z\left(= \frac{K_{II}}{K_I}\right) = \frac{-a \pm b\sqrt{a^2 - b^2 + 1}}{a^2 - b^2} \tag{24}$$

Only the negative solution of Eq. 24 is acceptable since $\theta_0$ must be between -90 and 0. Using the definition of the mixity parameter,

$$Me = \frac{2}{\pi}\arctan\left(\frac{K_I}{K_{II}}\right) \tag{25}$$

Simplifying,

$$\frac{K_I}{K_{II}} = \frac{\sigma\sqrt{\pi a}\sin^2\beta}{\sigma\sqrt{\pi a}\sin\beta\cos\beta} = \tan\beta \tag{26}$$

Replacing Eq. 26 in Eq. 25 and equating to Eq. 24,

$$\frac{2}{\pi}\arctan\left(\frac{K_I}{K_{II}}\right) = \frac{2}{\pi}\arctan\left(\frac{a^2 - b^2}{-a \pm b\sqrt{a^2 - b^2 + 1}}\right)$$

$$\arctan(\tan\beta) = \arctan\left(\frac{a^2 - b^2}{-a \pm b\sqrt{a^2 - b^2 + 1}}\right)$$

$$\beta = \arctan\left(\frac{a^2 - b^2}{-a \pm b\sqrt{a^2 - b^2 + 1}}\right) \tag{27}$$

We can solve for $\theta_0$ as a function of $(\beta, B, \alpha)$ using Eq. 27 and Eq. 19a-19b.

**Onset of Failure.** To solve for the stress at the onset of failure, Eq. 13 is substituted in Eq. 15,

$$K_{Ic} = Y\sqrt{2\pi r_c}(\sigma_{\theta\theta})_c = \cos\frac{\theta_0}{2}\left[K_I\cos^2\frac{\theta_0}{2} - \frac{3}{2}K_{II}\sin\theta_0\right] + T\sqrt{2\pi r_c}\sin^2\theta_0$$
$$= K_I\cos^3\frac{\theta_0}{2} - \frac{3}{2}K_{II}\sin\theta_0\cos\frac{\theta_0}{2} + T\sqrt{2\pi r_c}\sin^2\theta_0 \quad [28]$$

Assuming onset of failure, where $\sigma_f$ is the critical remote applied stress. and

$$K_I = K_{If} = \sigma_f\sqrt{\pi a}\sin^2\beta \quad [29a]$$
$$K_{II} = K_{IIf} = \sigma_f\sqrt{\pi a}\cos\beta\sin\beta \quad [29b]$$
$$T = T = \sigma_f\sqrt{\pi a}\cos 2\beta \quad [29c]$$

We can substitute Eq. 29a-29c in Eq. 28,

$$Y\sqrt{2\pi r_c}(\sigma_{\theta\theta})_c = K_I\cos^3\frac{\theta_0}{2} - \frac{3}{2}K_{II}\sin\theta_0\cos\frac{\theta_0}{2} + T\sqrt{2\pi r_c}\sin^2\theta_0$$
$$= (\sigma_f\sqrt{\pi a}\sin^2\beta)\cos^3\frac{\theta_0}{2} - \frac{3}{2}(\sigma_f\sqrt{\pi a}\cos\beta\sin\beta)\sin\theta_0\cos\frac{\theta_0}{2} + (\sigma_f\sqrt{\pi a}\cos 2\beta)\sqrt{2\pi r_c}\sin^2\theta_0$$
$$\vdots$$
$$(\sigma_{\theta\theta})_c = \frac{\sigma_f}{Y}\left(\frac{X}{\alpha} - \frac{Q}{\alpha} + Z\right)$$
$$\frac{\sigma_f}{(\sigma_{\theta\theta})_c} = \frac{Y}{\left(\frac{X}{\alpha} - \frac{Q}{\alpha} + Z\right)} \quad [30]$$

where,

$$X = \sin^2\beta\cos^3\frac{\theta_0}{2}$$
$$Q = \frac{3}{2}\cos\beta\sin\beta\sin\theta_0\cos\frac{\theta_0}{2}$$
$$Z = \cos 2\beta\sin^2\theta_0$$

Eq. 30 gives the stress at failure normalized by the critical stress in pure mode I.

**Tensile-shear Stress Criterion.** A fracture criterion for linear-elastic failure that takes into account local tensile and shear contributions and assumes a preferred crack deflection angle can be formulated based on the following two assumptions:

1. The crack propagates in a radial direction $\theta_0$ perpendicular to the remote tensile load (directional condition).
2. Crack propagation initiates when the near field stress $\sigma_f(\theta_0)$, which is defined as a contribution of the tensile $\sigma_{\theta\theta}$ and shear $\tau_{r\theta}$ stresses at a distance $r_c$ from the crack tip, reaches the same critical value as in pure mode I fracture (failure condition).

Hence, the following failure and directional conditions define the onset of fracture,

$$\theta_0 = \frac{\pi}{2} - \beta \quad [31]$$
$$\sigma_f(\theta_0) = \frac{K_{Ic}}{\sqrt{2\pi r_c}} \quad [32]$$

where the critical stress is,

$$\sigma_f^2 = \sigma_{\theta\theta}^2 + \lambda\tau_{r\theta}^2 \quad [33]$$

Using Eq. 7 and plugging in Eq. 29a-29c, the critical tensile stress at the onset of failure is,

$$\begin{aligned}
(\sigma_{\theta\theta})_c &= \frac{1}{\sqrt{2\pi r_c}}\cos\frac{\theta_0}{2}\left[K_I\cos^2\frac{\theta_0}{2} - \frac{3}{2}K_{II}\sin\theta_0\right] + T\sin^2\theta_0 + O(r^{1/2}) \\
(\sigma_{\theta\theta})_c &= \frac{\sigma_f\sqrt{\pi a}}{\sqrt{2\pi r_c}}\cos\frac{\theta_0}{2}\left[\sin^2\beta\cos^2\frac{\theta_0}{2} - \frac{3}{2}\cos\beta\sin\beta\sin\theta_0\right] + \sigma_f\cos(2\beta)\sin^2\theta_0 \\
(\sigma_{\theta\theta})_c &= \sigma_f\left[\frac{\sin^2\beta\cos^3\frac{\theta_0}{2} - \frac{3}{2}\cos\beta\sin\beta\sin\theta_0\cos\frac{\theta_0}{2}}{\alpha} + \cos(2\beta)\sin^2\theta_0\right] \\
(\sigma_{\theta\theta})_c &= \sigma_f A(\beta,\theta_0,\alpha) \quad [34]
\end{aligned}$$

Similarly, using Eq. 8 and plugging in Eq. 29a-29c, the critical shear stress at the onset of failure is,

$$\begin{aligned}
\tau_{r\theta} &= \frac{1}{2\sqrt{2\pi r}}\cos\frac{\theta}{2}\left[K_I\sin\theta + K_{II}(3\cos\theta - 1)\right] - T\cos\theta\sin\theta + O(r^{1/2}) \\
(\tau_{r\theta})_c &= \frac{\sigma_f\sqrt{\pi a}}{2\sqrt{2\pi r_c}}\cos\frac{\theta_0}{2}\left[\sin^2\beta\sin\theta_0 + \cos\beta\sin\beta(3\cos\theta_0 - 1)\right] - \sigma_f\cos(2\beta)\cos\theta_0\sin\theta_0 \\
(\tau_{r\theta})_c &= \sigma_f\left[\frac{\sin^2\beta\sin\theta_0\cos\frac{\theta_0}{2} - \cos\beta\sin\beta\cos\frac{\theta_0}{2}(3\cos\theta_0 - 1)}{2\alpha} - \cos(2\beta)\cos\theta_0\sin\theta_0\right] \\
(\tau_{r\theta})_c &= \sigma_f B(\beta,\theta_0,\alpha) \quad [35]
\end{aligned}$$

Using Eq. 32 and replacing Eq. 35 and Eq. 34, the critical stress normalized by the fracture toughness of the material can be calculated as a function of the local stress near the crack tip,

$$\begin{aligned}
\frac{K_{Ic}}{\sqrt{2\pi r_c}} &= \sqrt{(\sigma_{\theta\theta}^2 + \lambda\tau_{r\theta}^2)\Big|_{\theta_0}} \\
\frac{K_{Ic}^2}{2\pi r_c} &= (\sigma_{\theta\theta}^2 + \lambda\tau_{r\theta}^2)\Big|_{\theta_0} \\
\frac{K_{Ic}^2}{2\pi r_c} &= (\sigma_f A)^2\big|_{\theta_0} + \lambda(\sigma_f B)^2\Big|_{\theta_0} \\
\frac{\sigma_f}{K_{Ic}} &= \left.\frac{1}{\sqrt{2\pi r_c(A+\lambda B)^2}}\right|_{\theta_0} \quad [36]
\end{aligned}$$

The weighting factor $\lambda$ is assumed to be 1; that is, local tensile and shear stresses have equal contributions; tensile stresses dominate since they have a much greater magnitude compared to shear stresses. The geometry of finite specimens has an effect on the crack tip stress fields, and so expressions for stress intensity factors must be modified by the addition of a correction factor to enable their use in practical applications (2). Hence,

$$K_c = Y\sigma_c\sqrt{\pi a} \quad [37]$$

In the case of center-notched tension specimens (2),

$$Y = \sqrt{\sec\frac{a}{W}} \quad [38]$$

## 8. Finite Element Modeling

To perform numerical simulations on the hollow-tube octet nanolattices, we created finite element models of the as-designed notched and unnotched samples by using HyperWorks/Hypermesh (Fig. S11). Fig. S11B shows the side view for the FE model of a representative tensile nanolattice sample with an inclined center through-notch that also contains 918 octet-truss unit cells (27 (height) x 17 (width) x 2 (thickness)). The dimensions of the whole FE model are that the height is $127.44\mu m$, the width is $81.22\mu m$ and the thickness is $10.42\mu m$. Fig. S11C shows the zoomed-in side view of the FE model near the notch root. The FE model for the unit cell is shown in Fig. S11E. The length of the unit cell is taken as 4.72 um, the outer diameter of the hollow-tubes as $0.982\mu um$ and the thickness of the tube wall as $50nm$.

In describing the stress field at the notch root in the nanolattice sample, we have proposed a modified stress intensity factor, which is defined as $K_{IC} = K_{IC}A_g/A_n$ , where $A_g$ is the gross cross-sectional area and $A_n$ is the net cross-sectional area of the unnotched nanolattice sample. The gross cross-sectional area is the total width times the total thickness of the sample; while the net cross-sectional area of the sample is defined as the summation of all the tube wall cross-sectional areas across the nodal plane orthogonal to the loading direction. Within the unit cell, the net cross-sectional area is marked in blue as shown Fig. S11D.

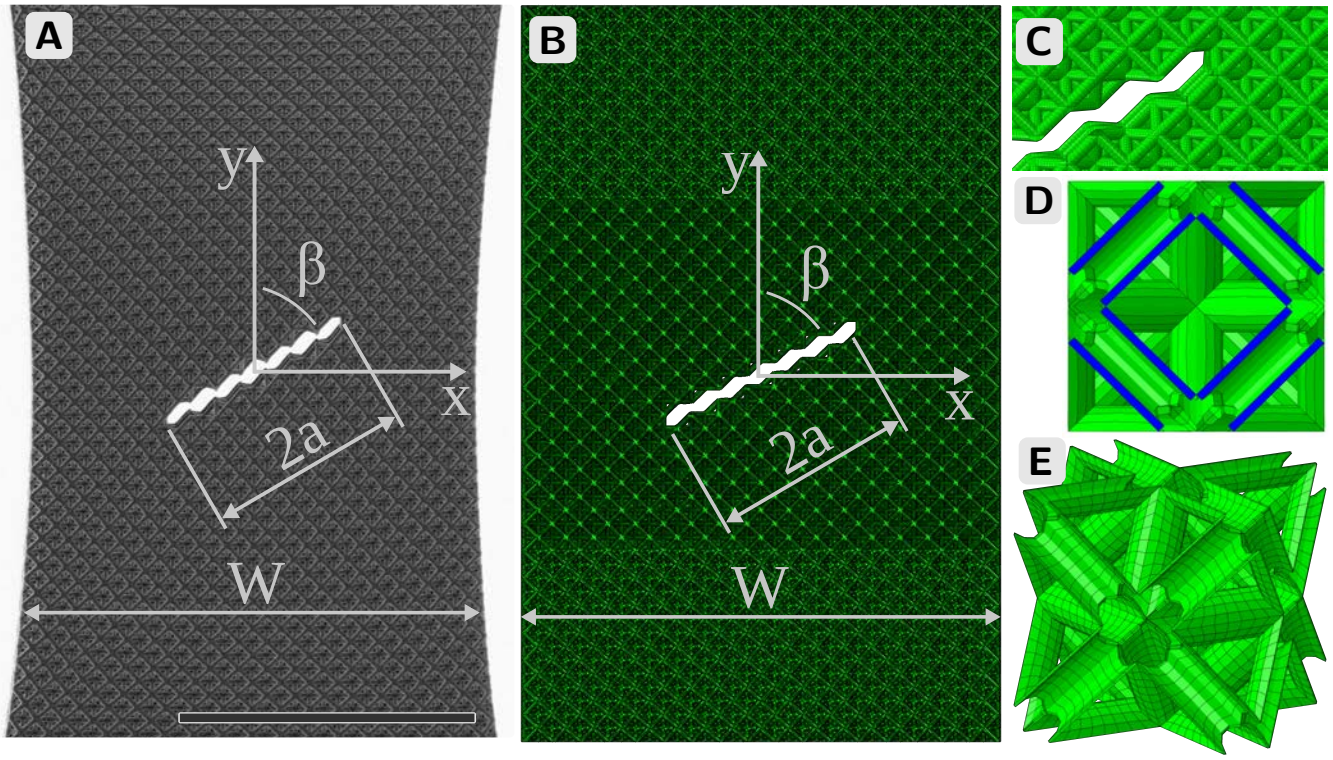


**Fig. S11.** Finite element models resembling as-fabricated center-notched tensile geometries. (A-C) SEM image and corresponding finite element model. (D-E) Octet unit cells are composed of shell elements.

Three dimensional 4-node quadrilateral shell elements with reduced-integration were employed to describe the octet hollow tube nanolattice samples. The material properties of ceramic $Al_2O_3$ for the FE analysis were obtained from the nanomechanical experiments of nano-pillars of $Al_2O_3$. In this work, the Young's modulus and ultimate tensile strength of $Al_2O_3$ were taken to be $165GPa$ and $5.166GPa$, respectively. A linear post-cracking stress-strain relationship was utilized in the FE simulations to describe the brittle damage evolution of $Al_2O_3$ hollow tubes leading to eventual failure. Contact behavior between the hollow tubes within the octet nanolattices was also considered in the FE simulations. Explicit dynamics procedure

was adopted to simulate the quasi-static uniaxial tensile loading applied to the notched and unnotched nanolattice samples. In order to ensure a quasi-static simulation, the kinetic energy of the whole system is kept to be less than 1% of the total internal energy. Hence, the effect of the kinetic energy of the system was negligible compared to its internal energy and external work. A post-processing module (ABAQUS/Viewer) was used to view the analysis results, e.g. reaction forces of nodes, stresses, and strains.

These numerical results along with the experimental analysis imply that failure of the hollow octet nanolattices occurs solely by means of tube wall fracture, in the absence of buckling, and the fact that failure propagation trajectory is always orthogonal to the loading direction implies that Mode I fracture plays a dominant role in brittle fracture of these hollow nanolattices. Failure surface morphology and stress-strain response obtained from experiments and finite element simulations closely resemble one another and demonstrate that initial failure always occurred at the nodal junctions with the highest local stress concentrations – at the notch roots in the flaw-containing samples and at the gauge section edges in the unnotched ones – by tearing of the $50nm$-thick alumina nodal junction walls. After this incipient tube wall tearing, global fracture occurred via brittle fracture of all nodal junctions within parallel lattice planes that emanate from the initially highest stress concentrations that are oriented orthogonally to the applied load, forming fracture planes.

Finite element simulations also enabled the evaluation of crack propagation path as a function of notch geometry and loading conditions. Fig. S12 contains FE-generated images of the nanolattice gauge sections with all six notch orientations, with crack propagation contours generated by FE simulations at different strains. The crack deflection plot and these profiles demonstrate that cracks always extend from the notch roots along the axis of the hollow beams towards the adjacent nodes, and follow a nodal lattice plane that is orthogonal to the loading direction. This failure mechanism stems from the lattice architecture: it provides a percolating surface of least resistance along the nearest-neighbor nodes, which depends on its connectivity. This failure mechanism of nodal-driven fracture is materials- rather than structure-based and marks a key distinction in crack propagation through continuum solids versus architected materials. After the initial failure, the pre-defined lattice connectivity drives subsequent rupture such that the fractured surface is oriented orthogonally to the loading direction regardless of the notch orientation. Simulations indicate that cracks emanate from the notch roots. Our numerical simulations revealed that the critical strain of $\varepsilon = 2.256\%$ was the highest for the unnotched sample and decreased monotonically from$\varepsilon = 1.844\%$ to $\varepsilon = 0.627\%$ for the notched samples as the center notch orientation varied from 0 to 90 degrees with respect to the loading direction. Once cracks start to propagate, the maximum stress concentration shifts to the nodes along the nodal plane orthogonal to the loading direction. Since the nodal junctions are the weakest links of the nanolattice structures, the nodal junction failure along the nodal plane orthogonal to the loading direction become inevitable. This mechanism also drives fracture in the unnotched nanolattices. The above analysis supports the experimental observations and suggests that crack propagation deflection is a direct consequence of the discrete nature of architected materials. Finite element analysis revealed the detailed information on the stress distribution in hollow-tube octet lattices, where the crack initiated at a node near the notch root and propagated through the nodes aligned with the plane orthogonal to the applied load.

**Calculation of the stress intensity factor.** For a typical center-through notch tension specimen as shown in Fig. S10, the solution for stress intensity factor is given by a polynomial expression (1, 2) as follows,

$$K_I = \frac{P}{T\sqrt{W}}\sqrt{\frac{\pi a}{4W}\sec\frac{\pi a}{2W}}\left[1 - 0.025\left(\frac{a}{W}\right)^2 + 0.06\left(\frac{a}{W}\right)^4\right] \quad [39]$$

where $P$ is the applied tensile force, $2a$ is the length of the characteristic notch oriented at 90 degrees,

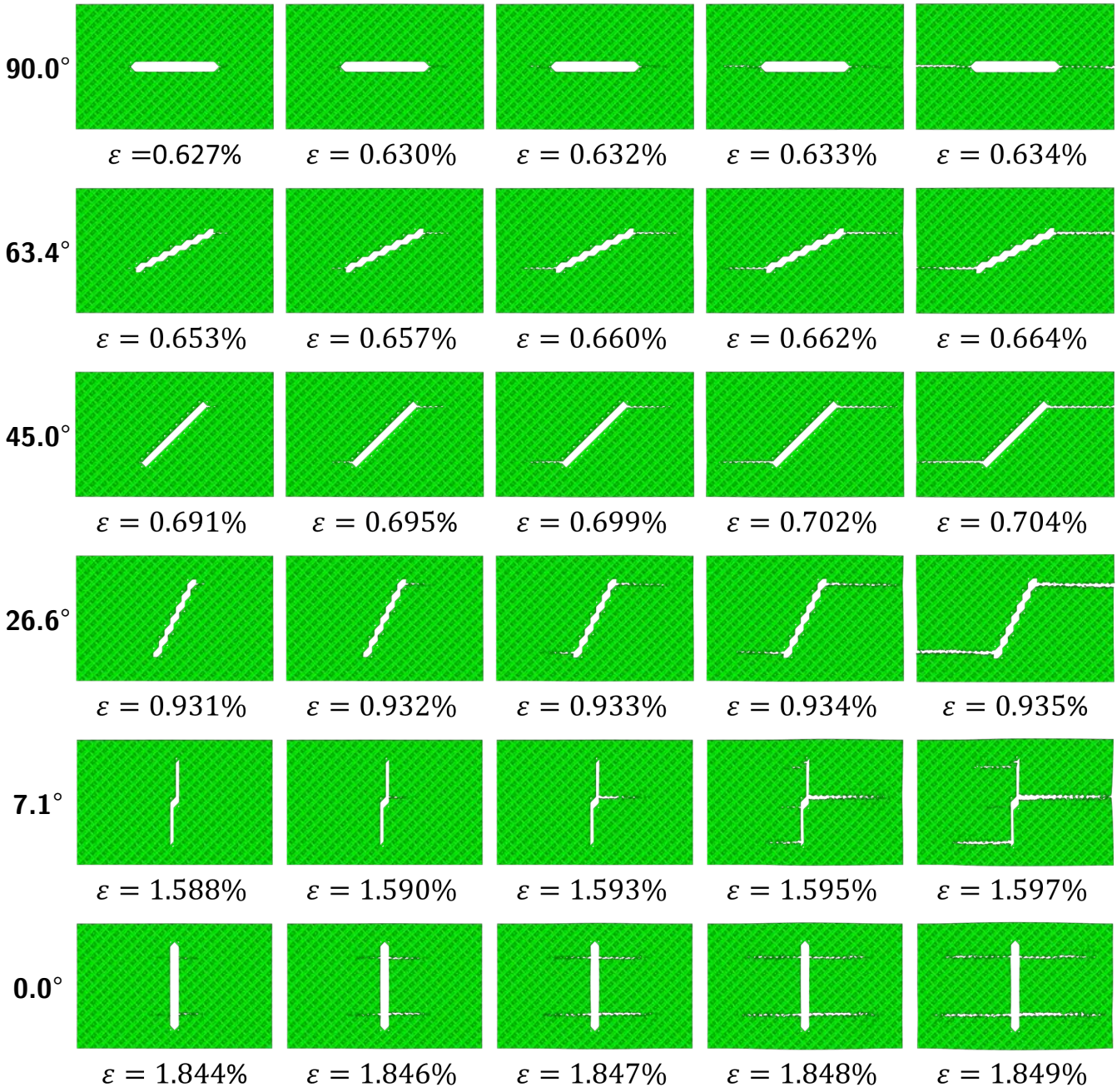


**Fig. S12.** Failure propagation paths as a progressing of applied strain of all notched nanolattices subjected to uniaxial tensile loading.

$2W$ is the width of this specimen, $T$ is the thickness of this specimen, and $\frac{P}{T\sqrt{W}} = \frac{P}{A}$ is the characteristic average stress applied to the specimen, and $A$ is the cross-sectional area of the specimen.

Based on the classical Mode I fracture model, the gross cross-sectional area of the hollow-tube octet architected nanolattice sample is taken to be $846.50\mu m^2$, and thus the classical stress intensity factor for the octet nanolattice sample at the maximal load was calculated as $K_I = 2.22MPa\sqrt{mm}$.

Based on the modified Mode I fracture model, the net cross-sectional area is found to be $36.47\mu m^2$, and then the modified stress intensity factor for the octet nanolattice sample was calculated as $K_I =$

$49.496 MPa\sqrt{mm}$.

The experimental, FE-simulation and effective notch length (ENL) criterion prediction results for the tensile strength of the hollow-tube octet nanolattice samples with center through-notches oriented at 6 different angles from 0 to 90 degrees are listed in Table S3.

**Table S3. Experimental, FE-generated, and ENL prediction results for the tensile strength of octet nanolattice samples with center through-notches with varying orientation angles**

| Notch orientation [°] | Tensile failure strength [$MPa$] | | |
|---|---|---|---|
| | Experiments | Simulations | ENL criterion |
| 90.0 | 7.22 | 8.20 | 8.20 |
| 63.4 | 7.14 | 8.96 | 9.02 |
| 45.0 | 8.51 | 10.09 | 10.15 |
| 26.6 | 11.22 | 14.71 | 13.21 |
| 7.1 | 19.15 | 26.78 | 25.93 |
| 0.0 | 26.74 | 31.10 | 29.16 |

## 9. Videos

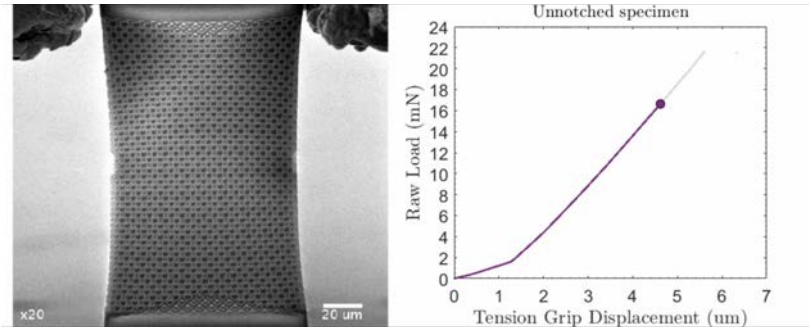


**VIDEO S1:** In-situ nanomechanical experiment of unnotched sample with corresponding load-displacement data.

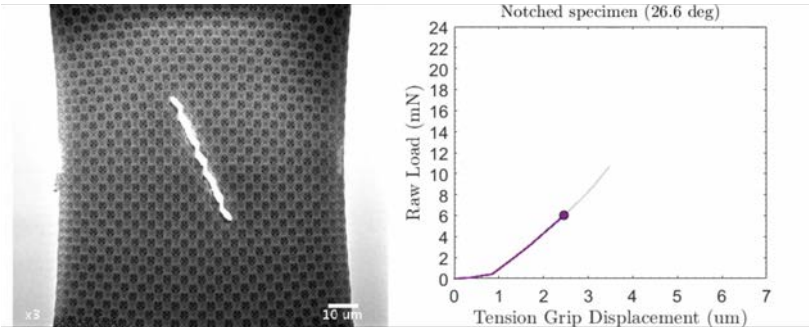


**VIDEO S2:** In-situ nanomechanical experiment of notched sample with corresponding load-displacement data.

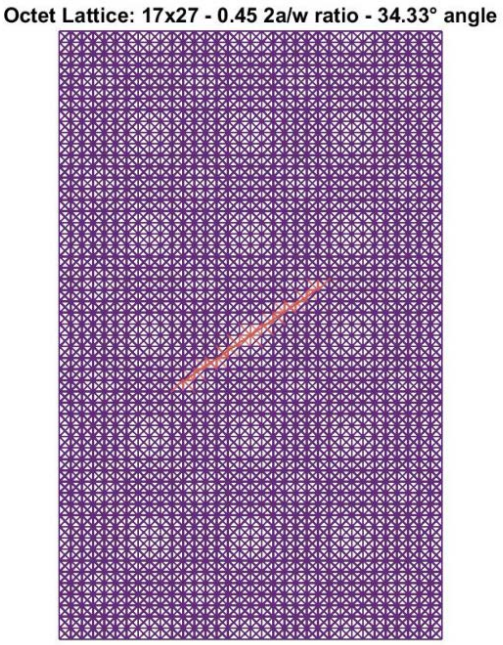


**VIDEO S3:** Visualization of MATLAB script capable of generating a lattice geometry with a center notch of varying orientation.

## 10. References


1. Gross D, Seelig T (2011) *Fracture Mechanics.* (Springer).
2. Broek D (1982) *Elementary Engineering Fracture Mechanics.* (Springer).
3. Begley MR, Hutchinson JW (2017) *The Mechanics and Reliability of Films, Multilayers and Coatings.* (Cambridge University Press).
4. Erdogan F, Sih GC (1963) On the crack extension in plates under plane loading and transverse shear. *Journal of Basic Engineering* 85(4):519–525.
5. Sih GC, Paris PC, Erdogan F (1962) Crack-tip, stress-intensity factors for plane extension and plate bending problems. *Journal of Applied Mechanics* 29(2):306–312.
6. Meza LR, Das S, Greer JR (2014) Strong, lightweight, and recoverable three-dimensional ceramic nanolattices. *Science* 345(6202):1322–1326.